Journal of Materials Chemistry C

ROYAL SOCIETY OF CHEMISTRY

PAPER

View Article Online
View Journal | View Issue

Cite this: J. Mater. Chem. C, 2026, 14, 7709

Synthesis and characterization of Cs_2TeCl_6 powder for scintillators

Lenka Prouzová Procházková,*[ab] Robert Král,[a] Mikhail G. Brik,[cdef] Eva Mihóková,[a] Romana Kučerková,[a] Vítězslav Jarý,[a] Vladimir Babin,[a] František Hájek[a] and Martin Nikl*[a]

Received 22nd December 2025,
Accepted 23rd February 2026

DOI: 10.1039/d5tc04464b

rsc.li/materials-c

We prepare powdered lead-free perovskite Cs_2TeCl_6 using a very simple hydrothermal method. We study in detail the luminescence mechanism and characteristics of Cs_2TeCl_6 (CTC) *via* both the measurement and phenomenological modelling of emission spectra and decays in a broad temperature interval of 77–500 K. Theoretical DFT calculations of the electronic band structure and exciton state were performed and discussed together with the experimental results. Radioluminescence spectra at room temperature provide an estimate of the CTC overall scintillation efficiency. Both the electron paramagnetic resonance and thermally stimulated luminescence characteristics give an insight into the energy transport in the CTC lattice and the involved charge carrier traps negatively affecting the scintillation performance. The concerted use of a broad portfolio of experimental and theoretical techniques provides a deep insight into the scintillation mechanism of CTC, and its intrinsic limits and bottlenecks. This powder scintillator, in combination with a suitable host matrix, could be an interesting material for double-beta decay detection.

1. Introduction

Recently, interest in the development and study of alternatives to lead perovskites has been growing as publications on preparation of lead-free perovskites have been appearing for several years.[1–3] Cesium lead bromide ($CsPbBr_3$, denoted as CPB) from a family of perovskites with general formula $A^+B^{2+}X_3^-$ (where A = Rb, Cs; B = Pb; and X = F, Cl, Br, and I) is a very promising material for many applications. However, it turns out that one of the crucial problems is the toxicity of Pb[4–6] and low structural stability,[7] especially due to its solubility in water and oxidation of the metal cation $Me^{2+} \rightarrow Me^{4+}$. For practical use, its low light yield (LY), due to strong self-absorption, also represents a limitation. The stability can be significantly improved by surface modifications, *i.e.* by silica coating[8] or stabilization in an appropriate host matrix.[9] The problem of toxicity must also be considered for new materials being developed, since their application will be governed by EU standards for the use of toxic elements in electronics.[1] The goal is to preserve the beneficial properties of lead halide perovskites stemming mainly from the electronic structure (lone-pair Pb $6s^2$ electrons and an empty Pb 6p orbital), large size (or crystal radius) and high effective mass (Z_{eff}), contributing to strong spin–orbit coupling and leading to high optical absorption and only shallow defects observable in the lead halide perovskites.[1] For this reason, metal cations with lone pair s orbitals, such as In^+, Tl^+, Ge^{2+}, Sn^{2+}, Bi^{3+} and Sb^{3+}, are proposed as a potential replacement for Pb. From this group, Tl and Sb are highly toxic metals; Bi, Sn and Ge are non-toxic. Sn^{2+} should be an appropriate candidate due to its very low toxicity and similar physical properties to Pb, but $ASnX_3$ perovskites showed inferior performance.[10] The structure of $A^+B^{2+}X_3$ perovskites can be advantageously replaced by the structure of the so-called double perovskite, $A_2^+B^{4+}X_6$; for example, $CsSn^{2+}X_3$ is susceptible to oxidation, while $Cs_2Sn^{4+}X_6$ is very stable when exposed to air and moisture. Unfortunately, it shows no or poor luminescence, unless it is doped with other elements (Bi^{3+}, Sb^{3+}, and Te^{4+}).[1] Another option is to replace Pb with two metals with different valencies ($A_2B^+B^{3+}X_6$) to yield the same overall charge balance as conventional perovskites. Both structures have been proposed as structurally stable, lead-free ("green") materials with promising optical and luminescence properties.[3] The structure of $A_2^+B^{4+}X_6$ is usually considered as vacancy-ordered double perovskite, where the B cation is partially replaced with a vacancy (B = Sn, Ti, Te and Pd),[11] possessing good structural stability.[3] Empirical modelling predicted the lattice constants for a series

[a] Institute of Physics of the Czech Academy of Sciences, Cukrovarnicka 10, 162 00 Prague, Czech Republic. E-mail: nikl@fzu.cz, prochle2@fjfi.cvut.cz
[b] Czech Technical University in Prague, Faculty of Nuclear Sciences and Physical Engineering, Břehová 7, 115 19, Czech Republic
[c] School of Integrated Circuits & CQUPT-BUL Innovation Institute, Chongqing University of Posts and Telecommunications, Chongqing, 400065, China
[d] Center of Excellence for Photoconversion, Vinča Institute of Nuclear Sciences – National Institute of the Republic of Serbia, University of Belgrade, Belgrade, Serbia
[e] Institute of Physics, University of Tartu, W. Ostwald Str. 1, Tartu, 50411, Estonia
[f] Academy of Romanian Scientists, 3 Ilfov, 050044, Bucharest, Romania

of cubic structures with A_2BX_6 composition as already published in ref. 12, where the data from the model were compared with crystallographic data. More information about halide double perovskites is provided in reviews.[1,3] Cs_2SnI_6 or Cs_2SnCl_6 vacancy-ordered perovskites were studied as prospective lead-free perovskites for solar cell applications[13,14] exhibiting poor photoluminescence (PL) and low photoluminescence quantum yield (PLQY). It was shown that $A_2Sn^{4+}X_6$ is not suitable for absorber layer application in solar cells because of high Sn vacancy density.[13] Several other tetravalent ions, such as Ti^{4+}, Zr^{4+}, Hf^{4+}, Pd^{4+} and Te^{4+}, can replace Sn^{4+} in the perovskite structure.[14,15] The defect formation energy was evaluated for verification of the ability to replace Sn^{4+} ions by Te^{4+} (partially or completely) in the Cs_2SnI_6 structure.[11] The synthesized solid solution $Cs_2Sn_{1-x}Te_xI_6$ showed increasing defect intolerance with increasing Te concentration. Furthermore, the studied $Cs_2Sn_{1-x}Te_xI_6$ solid solutions exhibited poor thermal stability and the PL quenched completely at 323 K. The dopant correlated luminescence mechanism of Te^{4+}-doped Cs_2SnCl_6 was investigated through analysis of the absorption, emission/excitation, and time-resolved PL spectroscopy.[16] It was believed that green-yellow emission in Cs_2SnCl_6:Te^{4+} originates from the synergic contribution of the Te^{4+} ion triplet ($^3P_1 \rightarrow {}^1S_0$) transition and self-trapped exciton (STE) recombination, which is analogous to the interpretation of luminescence characteristics in the Tl^+-doped CsX crystals.[17] The energy gap decreases with the increased ratios of Te/Sn. Pure Cs_2TeCl_6 (CTC) appears to have the smallest energy gap: the PL position is at 590 nm and the PLQY is low. It is interpreted as being due to high Te-doping concentration, causing concentration quenching, resulting from a critical distance of $[TeCl_6]^{2-}$–$[TeCl_6]^{2-}$ groups in the energy transfer process, calculated to be three times longer than the shortest Te–Te distance.[18]

Tellurium-based halide perovskites have been studied more in recent years and their optical, electronic and luminescence properties were described.[16,19,20] Tellurium is known for its physicochemical properties – it is a nonmetallic element with the strongest metallic properties. Te is considered less toxic than Pb, but this only applies to inorganic compounds. Organic Te compounds and their vapours are highly toxic, which could be rather limiting for synthesis of Te-based halides. Usually, the synthesis is carried out *via* a solvothermal route using inorganic compounds, such as oxides or chlorides dissolved in hydrochloric acid.[21,22] Te-based halide perovskites possess some advantageous properties, such as a large absorption cross-section, a wide emission band in the yellow spectral region and good structural as well as chemical stability. Theoretical data of structural stability and basic optical and electronic properties of Cs_2TeX_6 calculated from first-principles were reported.[20] The stability of the three studied Te-based perovskites increases in the sequence $Cs_2TeI_6 < Cs_2TeBr_6 < Cs_2TeCl_6$. As CTC features only poor luminescence properties and low PLQY, doping with various ions (Cr^{3+}, Mn^{2+}, Yb^{3+}, Eu^{3+}, Sm^{3+}, Cd^{3+}, Bi^{3+}, and Ce^{3+}) was studied.[19] It was shown that Cr^{3+} doping leads to the improvement of PLQY from 6.7% to 81.5%. Such materials can have prospective use in white light emitting diode applications.

It is worth noting that Te-doped metal halides exhibit extremely high PLQY (*e.g.*, 95.4% for Te doped Cs_2SnCl_6[23] and 97.6% for the Te-doped Cs_2ZrCl_6[24]). The mechanism of luminescence of Te-based or Te-doped metal halides remains unclear. It was shown[25] that admission of Hf in the CTC structure significantly improved scintillation properties; the PLQY increased from 3% to 97% and the LY increased nearly tenfold from ≈4167 to 38 523 photons per MeV.

The use of tellurium-based scintillators is of potential interest especially due to the neutrino-less double beta decay detection. Isotope ^{130}Te has large natural abundance (34%), so natural compounds do not need further enrichment. ^{130}Te double beta decay half-lives measured over decades in different laboratories usually provide two different values: $2.5 \pm 0.4 \times 10^{21}$ years and $8 \pm 1 \times 10^{20}$ years.[26] The geochemical method of measuring double beta decay depends on the detection of the rare gas daughter that has accumulated in geologically old minerals from ββ-decay of the parent nuclide:[27]

$$^{130}\mathrm{Te} \xrightarrow{\beta\beta} {}^{130}\mathrm{Xe}$$

$$^{128}\mathrm{Te} \xrightarrow{\beta\beta} {}^{128}\mathrm{Xe}$$

Recently, efforts to incorporate tellurium directly into scintillation cocktails have been noted,[28] and so the preparation of a scintillator containing tellurium would be an interesting alternative.

In this paper we study in detail the luminescence mechanism of CTC *via* the measurement of emission spectra and decays in a broad temperature interval 77–500 K and their phenomenological modelling. Theoretical DFT calculations of the electronic band structure and exciton state are provided and discussed together with experimental results. Radioluminescence spectra and decay at room temperature provide an estimate of the CTC overall scintillation efficiency and speed of scintillation response, respectively. Both the electron paramagnetic resonance and thermally stimulated luminescence characteristics give an insight into the energy transport in the CTC lattice and charge carrier traps negatively affecting the scintillation performance. The concerted use of such a broad portfolio of experimental and theoretical techniques provides a deep insight into luminescence and scintillation mechanism of CTC, and its intrinsic limits and bottlenecks.

2. Experimental

2.1. Synthesis

The synthesis of Cs_2TeCl_6 in the microcrystalline powder form followed the method description in ref. 22, which was based on the hydrothermal reaction of tellurium oxide (TeO_2, Merck, 99.995%) and cesium chloride (CsCl, purified *via* a combination of chlorination agents and zone refining) dissolved in hydrochloric acid (HCl) at 110 °C for 6 hours. This led to the CTC synthesis and its precipitation into a microcrystalline solid product. The solid phase was then separated *via* microfiltration and dried at 60 °C. This experiment was repeated for verification of results; for more information see the SI.

In the next step, attempts to reduce the particle size by synthesis modification were carried out. However, the solid CTC product was formed directly after the mixing of dissolved precursors while following the procedure described in ref. 22. Therefore, the procedure was modified by omitting the hydrothermal step and synthesizing the CTC from the precursors (CsCl and TeO_2) diluted in HCl by their dropwise direct mixing. The suspension was mixed for 20 hours, and the product was then separated *via* microfiltration. The sample prepared by this simplified procedure was further used for luminescence characterization. The comparison of sample properties is provided in the SI (Fig. SI1, SI3 and Tables SI1, SI2).

2.2. Methods of characterization

X-ray powder diffraction (XRPD) was used for structural and phase purity confirmation. XRPD was performed using Rigaku MiniFlex 600 (Ni-filtered Cu-Kα1,2 radiation) equipped with a NaI:Tl scintillation detector and diffractograms were compared to the relevant records in the ICDD PDF-2 database (version 2013). The morphology characterization was performed using scanning electron microscopy (SEM, Philips XL30ESEM).

Radioluminescence (RL) spectra were measured using a custom-made spectrofluorometer 5000 M (Horiba Jobin Yvon, Wildwood, MA, USA) using a W-based X-ray tube (40 kV, 15 mA, Seifert) as the excitation source. The detection part of the setup involved a single-grating monochromator and an Andor Kymera 193i spectrograph equipped with a back illuminated CCD detector iDus 420 (200–1100 nm spectral range). Measured spectra were corrected for the spectral dependence of detection sensitivity (RL).

Photoluminescence excitation (PLE) and photoluminescence emission (PL) spectra were measured using a custom-made spectrofluorometer 5000 M using a steady state laser driven xenon lamp (Energetiq, a Hamamatsu Company). PL decays were measured under excitation using a microsecond flashlamp and nanosecond nanoLED pulsed light sources using multichannel scaling and time-correlated single-photon counting mode (Horiba Scientific), respectively. The detection part of the setup involved a single-grating monochromator and a photon-counting detector TBX-04 (Hamamatsu). The PL and PLE spectra are corrected for the experimental distortion. The convolution procedure was applied to the PL decay curves to determine true decay times (SpectraSolve software package, Ames Photonics).

Temperatures within 77–500 K were controlled using a liquid nitrogen-bath variable temperature cryostat with the sample in a vacuum DN-V (Oxford Instruments).

The fast X-ray-excited spectrally unresolved scintillation decays are measured at room temperature by the time-correlated single-photon-counting method using a FluoroHub unit coupled with a hybrid photomultiplier HPPD-860, operated in the range of 220–860 nm (Horiba Jobin Yvon) together with a picosecond X-ray pulsed source at 40 kV N5084 (Hamamatsu) with a maximal frequency of 10 MHz. The FWHM of the instrumental response function of the setup is 75 ps.

The thermally stimulated luminescence (TSL) glow curves were measured using the Horiba Jobin Yvon 5000 M spectrometer with the liquid nitrogen cryostat (Oxford Instruments) and TBX-04 photomultiplier operating in the 200–800 nm spectral range (spectrally unresolved), or Andor Kymera 193i spectrograph equipped with a back illuminated CCD detector iDus 420 (within 200–1100 nm, spectrally resolved); the samples are irradiated using a Seifert X-ray tube with a tungsten target operated at 40 kV. The TSL is recorded during linear heating of the sample holder (typical ramp rate 0.1 K s^{-1}).

EPR measurements were performed using a commercial Bruker EMX plus spectrometer in the X-band (9.4 GHz) within the 10–296 K temperature range. The spectrometer sensitivity is about 1012 spins per mT at room temperature.

3. Theoretical calculations

Cs_2TeCl_6 crystallizes in a cubic structure, space group *Fm*3*m*, no. 225. The lattice constant is $a = 10.445$ Å, and there are four formula units per one-unit cell.[29] The calculations of its structural, electronic and optical properties were carried out using the CASTEP module[30] of the Materials Studio package.[31] The local density approximation (LDA) with the Ceperley–Alder–Perdew–Zunger (CA-PZ) functional[32] and the general gradient approximation (GGA) with the Perdew–Burke–Ernzerhof (PBE) functional[33] were employed. The plane-wave basis energy cutoff was 240 eV. The Monkhorst–Pack scheme *k*-point grid sampling was set at $4 \times 4 \times 4$; the convergence criteria were as follows: energy 10^{-5} eV per atom; maximal force 0.03 eV $Å^{-1}$ maximal stress 0.05 GPa and maximal displacement 10^{-3} Å. The electronic configurations were as follows: $5s^25p^66s^1$ for Cs; $5s^25p^4$ for Te, $3s^23p^5$ for Cl.

The optimized lattice constants were 10.9186 Å (GGA calculations) and 10.1257 Å (LDA calculations), the calculated indirect electronic band gaps were 2.760 eV (GGA) and 2.324 eV (LDA). These values are close to other calculated indirect band gaps of 3.1 eV[34] and 2.78 eV.[35] The calculated effective Mulliken charges were as follows (the GGA/LDA values are given): Cs +0.77/0.66; Te +1.38/+ 1.44, Cl −0.49/−0.46. A large difference between the formal and effective charges, especially for the Te and Cl ions, indicates a high degree of covalency of the Te–Cl chemical bond.

Fig. 1 shows the GGA-calculated band structure diagram for Cs_2TeCl_6 (the LDA results are not shown for the sake of brevity and clarity of the figure). The composition of the electronic bands can be clarified by analyzing the density of states (DOS) diagrams given in Fig. 2. The conduction band is made up of mainly the Te 5p states with a minor contribution of the Cs 6s states. The valence band between 0 eV and −2.5 eV is dominated by the Cl 3p states, whereas the top of the valence band also has some contribution from the 5p states of tellurium because of hybridization effects between Cl and Te ions. Highly hybridized Te 5p and Cl 3p states form another narrow band at about −4 eV. The 5s and 5p states of Cs show peaks at −19 eV and −7 eV, respectively. The 5s states of Te produce a narrow band at about −10 eV, and the Cl 3s states are spread between −15 and −12.5 eV.

The structure of the valence band with several sub-peaks within it, as well as the presence of several narrow electronic

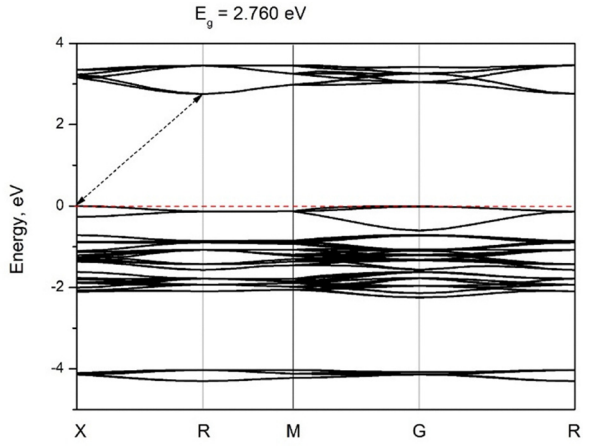

Fig. 1 The calculated (GGA) band structure of Cs_2TeCl_6. The indirect band gap is shown by a dashed arrow.

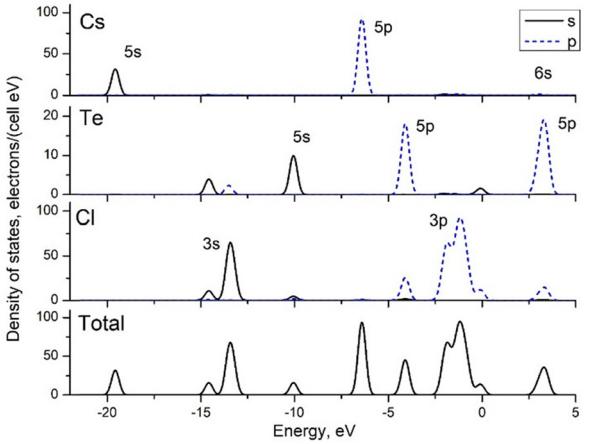

Fig. 2 The calculated (GGA) density of states (DOS) diagrams for Cs_2TeCl_6.

bands just below the valence band, is responsible for the structured absorption spectra of Cs_2TeCl_6.

After the electronic band structure of a solid is calculated and plotted, it is possible to estimate the effective mass of the charge carriers (electrons in the conduction band and holes in the valence band). To do that, one has to find the curvature of the electronic bands (or the second derivative of these bands over the wave vector k):

$$m^*_{h(e)} = \frac{\hbar^2}{d^2E_{v(c)}/dk^2}, \quad (1)$$

where h(e) denotes the holes (electrons), and the subscript v(c) stands for the upper (lower) energy bands in the valence (conduction) bands, respectively.

With the knowledge of the effective masses of electrons and holes, the exciton diameter a_0 can be calculated from the following equation:[36,37]

$$a_0 = \frac{2\hbar^2\varepsilon_\infty}{m^*e^2}, \quad (2)$$

where $m^* = \frac{m^*_h m^*_e}{m^*_h + m^*_e}$ is the charge carriers' reduced mass and ε_∞ is the dielectric constant value in the limit of infinite wavelength (according to ref. 35, its value is equal to three for Cs_2TeCl_6). With this value of the exciton diameter, the exciton binding energy E_b is

$$E_b = \frac{2\hbar^2}{m^*a_0^2}. \quad (3)$$

The results of estimations of all these parameters for Cs_2TeCl_6 are as follows: $m^*_e = 1.48m_e$ $m^*_h = 3m_e$; $m^* = 0.99m_e$; a_0 = 3.1 Å; E_b = 1.5 eV. It can be emphasized that the valence band top is remarkably flat, which leads to a very high value of the hole effective mass. A small effective exciton diameter and a rather high exciton binding energy indicate strong exciton localization in Cs_2TeCl_6. Presumably, due to a great positive charge of Te ions, the electron is likely to be localized on the tellurium ion in the center of the $TeCl_6$ octahedron, whereas the hole may diffuse between the nearest six chlorine ligands in the first coordination sphere around Te ions. Several other references also report similarly high values of exciton binding energies in highly covalent systems, for example, 0.7 eV in WS_2,[38] 0.69 eV in CrSBr,[39] 0.85 eV in phosphorene and 2.03 eV in graphene fluoride.[40]

The novelty of the performed calculations for Cs_2TeCl_6 is at least two-fold: (i) demonstration of a high degree of covalency of chemical bonds by comparing the effective Mulliken charges of all ions with their formal charges expected from the chemical formula; and (ii) estimation of the exciton diameter and exciton binding energy from the calculated electron band structure.

4. Experimental results and discussion

4.1. Structural properties

In total, three batches of CTC powder samples were prepared hydrothermally and by direct precipitation. All samples were bright yellow with sub-millimeter grain sizes containing no visible foreign phase.

The XRPD of Cs_2TeCl_6 powder samples (Fig. 3) confirmed the presence of a pure Cs_2TeCl_6 crystal phase belonging to the cubic space group *Fm*3*m* with a vacancy-ordered double perovskite structure (Fig. 3 inset), which is structurally derived from elpasolite CLYC (Cs_2LiYCl_6).[29] The diffraction patterns of samples prepared by direct precipitation at room temperature (Fig. 3) and hydrothermally at 110 °C showed no significant changes (see all XRPD data in the SI, Fig. SI1), which means that the CTC crystal phase was formed practically immediately after both solutions came into contact.

Lattice parameters and average crystallite size were calculated from XRPD data and are listed in the SI (Table SI1). Lattice parameter a = 10.4712 Å is in a relatively good agreement with values reported in the literature – the experimental value published already in 1935 by Engel is 10.445;[29] ref. 19 indicates the value 10.500 Å, while ref. 34 states the experimental value 10.5167 Å; the theoretical value calculated in ref. 41 is 10.497 Å. The experimental lattice parameter determined by us lies between those obtained by the GGA and LDA calculations

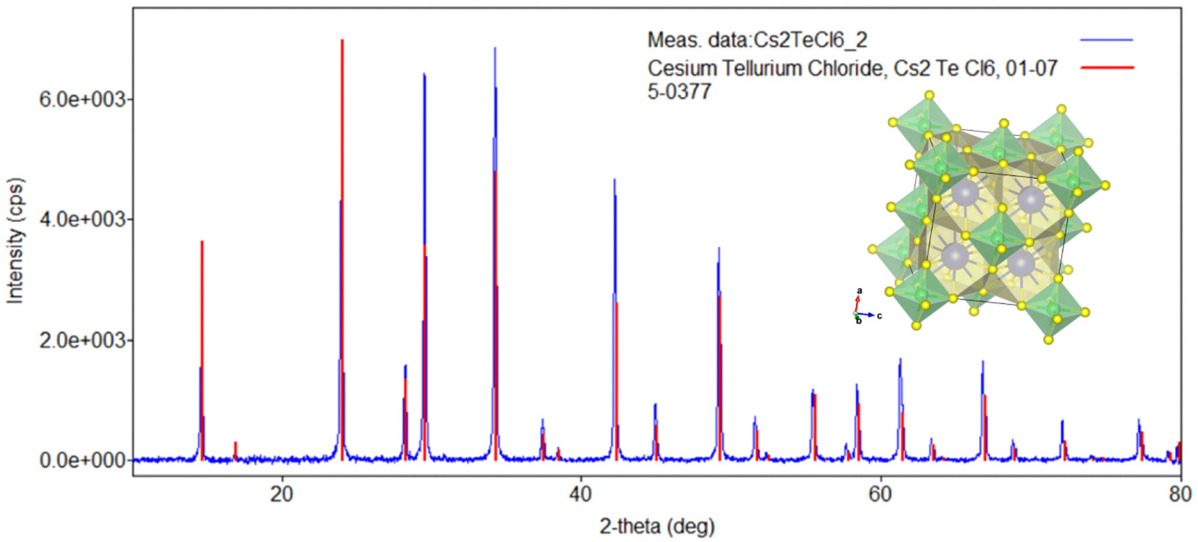

Fig. 3 XRD data of Cs_2TeCl_6 after direct precipitation from reaction solutions (Cs_2TeCl_6_3); the phase was analyzed as a cesium tellurium chloride in the perovskite structure (#01-075-0377); inset – cubic crystal structure of Cs_2TeCl_6; the Te^{4+} cations (green) are represented in the center of the octahedra, Cs^+ cations (blue-grey) are surrounded by eight octahedra, and Cl^- anions (yellow) are placed at the vertices of the octahedron.

described above. The average crystallite size calculated from XRPD was 524 nm, which was also confirmed by SEM images showing the microcrystalline nature of the powder CTC sample (Fig. 4a–d). SEM images also showed that the powder was partly composed of particles with an average size of several micrometers (Fig. 4d); sometimes crystallites with characteristic dimensions of 200–400 nm were observed as well. Fast degradation of samples was observed after one day of the SEM measurement. Crystallites were basically not observed anymore, only large smoother objects. Moreover, both samples turned completely black (as observed by the naked eye). In the following SEM images (Fig. 4e and f), noticeable degradation of crystallinity was observed, with clearly recognizable signs of water droplets. Given that, despite SEM measurements, they were not stored under special conditions, possibly their degradation and hygroscopicity were initiated by electron radiation.

4.2. Luminescence characteristics

Fig. 5 shows the normalized PL excitation and emission spectra of the CTC sample measured at 77 K (Fig. 5a) and RT (Fig. 5b).

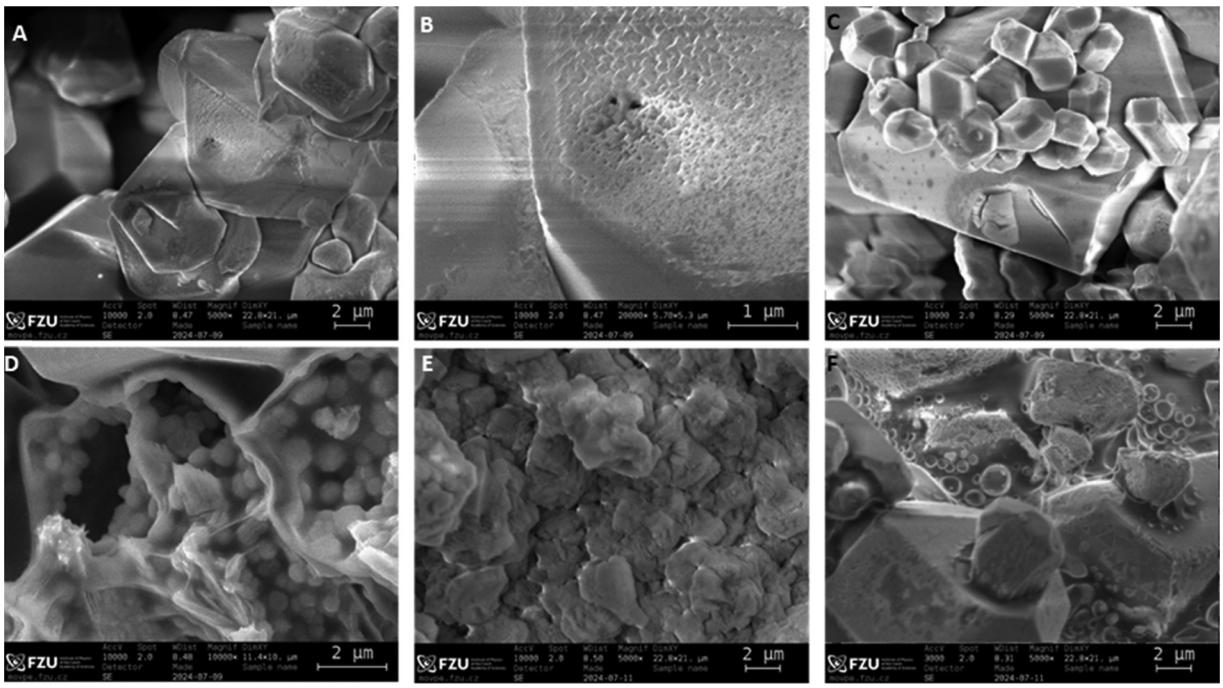

Fig. 4 SEM images of microcrystalline CTC powder (a–d – as prepared, e and f – one day after the first SEM measurement).

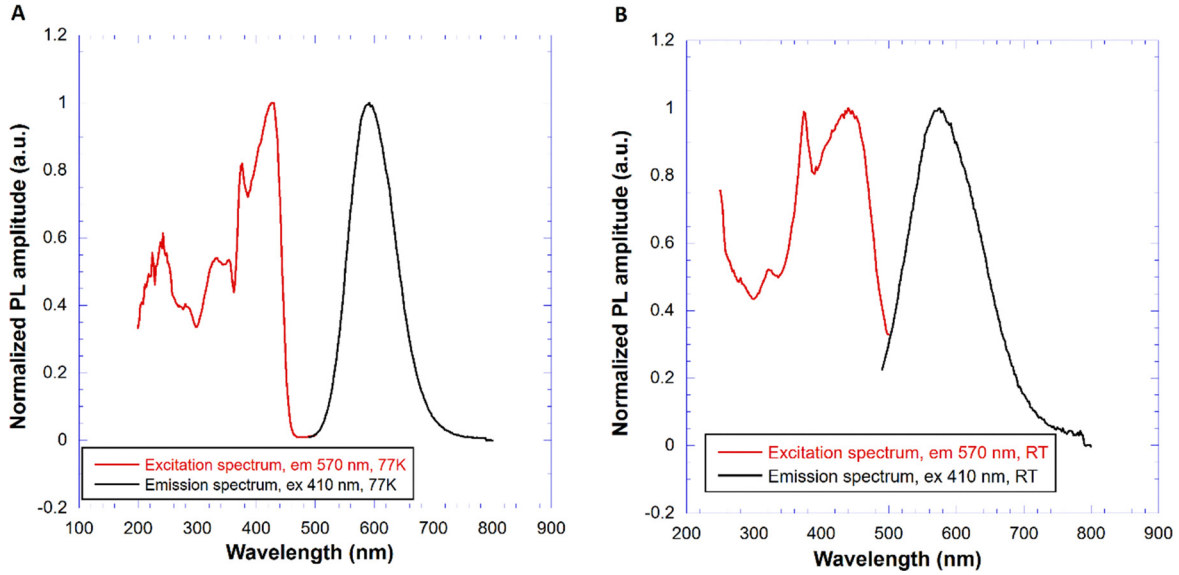

Fig. 5 (a) Normalized PL excitation (red curve) and emission (black curve) spectra of CTC measured at 77 K; (b) normalized PL excitation (red curve) and emission (black curve) spectra of CTC measured at RT.

Given the excitonic nature of the emission centre[16,19] the excitation long-wavelength edge could coincide with the absorption edge, *i.e.* around 440 nm and 460 nm at 77 K and RT, respectively, but the character of the band-to-band transition (Fig. 1) might somewhat obscure such a coincidence. The peak at 375 nm in PLE (Fig. 5a) does not shift with temperature and might be related to a particular feature of the density of states in the bottom of the valence band (Fig. 2). The structures of the PLE spectra at around 200–260 nm might be due to the onset of the multiplication of electronic excitation ($>2E_g$)[42] or the transitions from electronic bands located below the valence band to the conduction band. At 77 K there is clearly no overlap between the excitation and emission spectra in Fig. 5a which excludes exciton migration. At RT, however, due to the shift of the low energy edge of the excitation spectrum and broadening of the emission one, the spectra do overlap around 500 nm which was considered[18] as a reason for concentration quenching of exciton emission.

Representative RT PL decay curve (λ_{ex} = 452 nm, λ_{em} = 570 nm) of CTC is shown in Fig. 6. It is well approximated by a single-exponential with the decay time of 65.7 ns.

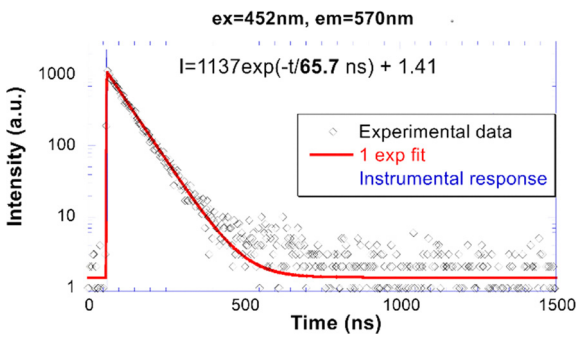

Fig. 6 RT PL decay curve (λ_{ex} = 452 nm, λ_{em} = 570 nm) of CTC. The solid line is the convolution of instrumental response and the function $I(t)$ in the figure.

4.3. Temperature dependences of PL spectra and decays

Temperature dependence of PL emission spectra of CTC under the 430 nm excitation in the low temperature region is shown in Fig. 7. Apart from the expected spectral broadening due to the interaction with lattice phonons there is a small high energy shift of the spectral maximum. At the same time the low energy shift of the excitation spectrum edge is visible from Fig. 5 which means that the Stokes shift becomes somewhat smaller with increasing temperature. In principle, there might be two reasons for such behaviour: (a) temperature dependence of the relaxation process into the self-trapped exciton state; (b) inhomogeneous broadening of the exciton emission, *i.e.* some effect of lattice defects or irregularities on the relaxed exciton state and earlier quenching of emission subbands at the low energy side of the emission band. This aspect needs further investigation.

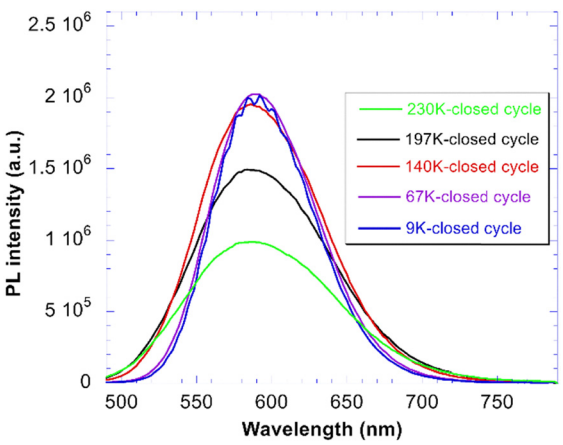

Fig. 7 Temperature dependence of PL emission spectra of CTC under the 430 nm excitation.

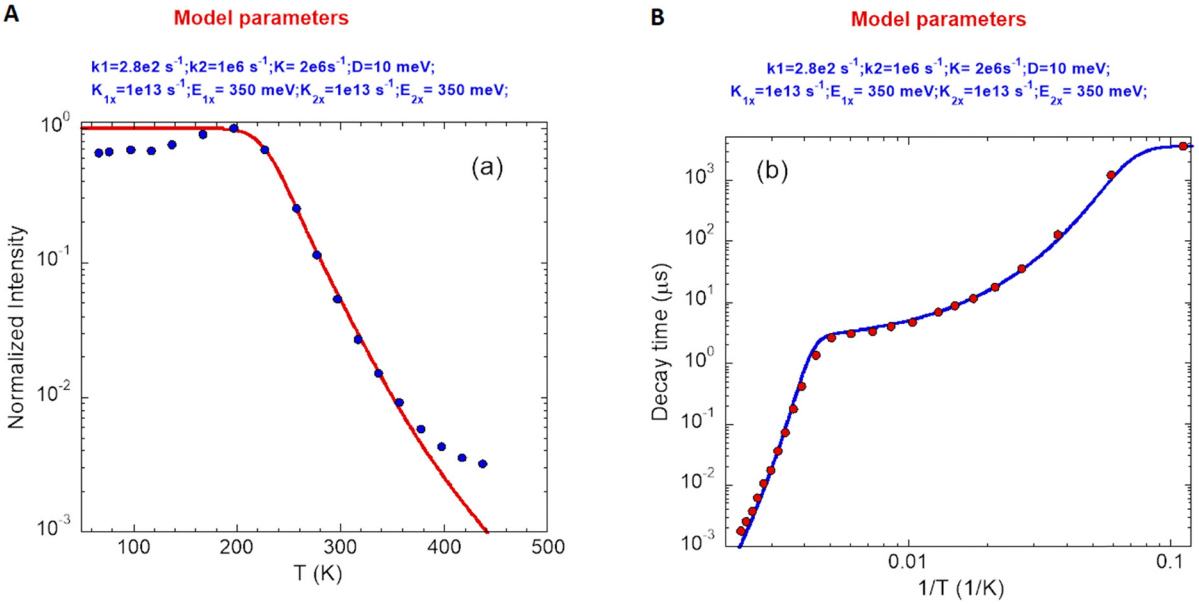

Fig. 8 (a) Temperature dependence of PL spectra integral within 480–750 nm, (b) PL decay times approximated by the phenomenological model displayed in Fig. SI2, see also the text.

Strong emission intensity quenching appears above 200 K. Temperature dependence of the emission spectra integrals is displayed in Fig. 8a. The mild increase of emission intensity within 77–200 K can be due to the shift of the absorption/excitation edge, see Fig. 5. Phenomenological two-excited-state level model is applied consistently to the temperature dependence of both the PL spectra integrals (Fig. 8a) and decay times (Fig. 8b). The model is sketched in SI, Fig. SI2, and consists of two closely spaced excited state levels frequently used for the description of temperature dependences of spectra and decays of excitons in halides.[17] More details are reported in the SI. The energy barrier for thermal quenching to the ground state is calculated to be 350 meV considering the quenching process occurring equally from both levels. PL yield at room temperature can be estimated from Fig. 8a: under the assumption that before the onset of temperature quenching around 200 K the luminescence quantum efficiency is close to 1, around room temperature, due to thermal quenching (included in the phenomenological model in Fig. SI2), it is about 0.05–0.07.

Fig. 8b demonstrates that the data can be excellently fit with the same model parameters (see values in Fig. 8a and b) supporting the model validity. Slowly decreasing decay time within 77–200 K points to two closely spaced levels in the exciton state which is typical for exciton emission in CsX halides.[17] Above 200 K the pronounced decay time shortening occurs and is consistent with the emission intensity quenching evidenced in Fig. 8a.

It is worth discussing further the nature of emission quenching above 200 K which was proposed to be due to concentration quenching[18] and considered in later publications, *e.g.* in ref. 16. From temperature dependence of emission spectra integral, the onset of quenching process occurs at about 200 K. The nature of concentration quenching lies in the energy migration over the donor (exciton) states until an acceptor (a quenching site) is reached. The process is energy diffusion-limited and as such obeys the Yokota–Tanimoto model.[43] PL decays in this case show a clearly accelerated initial part and an exponential tail. However, in our case, within the 200–300 K interval, where the emission intensity decreases by more than twenty times, the PL decays are strictly single exponential, see Fig. SI4. Such a feature of PL decays rules out the concentration quenching as an explanation of emission quenching. As the binding energy of the exciton state is large (calculated value in Section 2 is E_b = 1.5 eV) thermal disintegration of the exciton state as a reason for emission quenching is improbable, and thus the classical thermal quenching, *i.e.* transition from an excited state to the ground state *via* the crossing point of the respective parabolas (used in our two excited-state-level model), is the correct explanation.

4.4. Scintillation characteristics

Radioluminescence spectra (Ex = X-ray 40 kV, W-based tube) measured at both RT and 77 K temperatures are shown in Fig. 9 and severe emission intensity quenching is noted similar to that described for the PL spectra in Fig. 7. A characteristic broad emission band with maxima at around 590 nm is consistent with the PL spectra and thus attributed to the self-trapped exciton.[1,2,19] The highest RL intensity was observed in Cs_2TeCl_6 (Fig. SI3) possibly due to the formation of larger CTC (microsized) grains (see Fig. 4). A significant decrease of RL intensity between 77 K and RT is caused by the luminescence thermal quenching described in Section 4.3.

Spectrally unresolved scintillation decay curve of CTC recorded at RT under the X-ray excitation (40 kV) is shown in Fig. 10. It is approximated by the sum of exponentials in the following form:

$$I(t) = \sum_{i=1}^{n} A_i e^{-\frac{t}{\tau_i}} + \text{background} \quad (4)$$

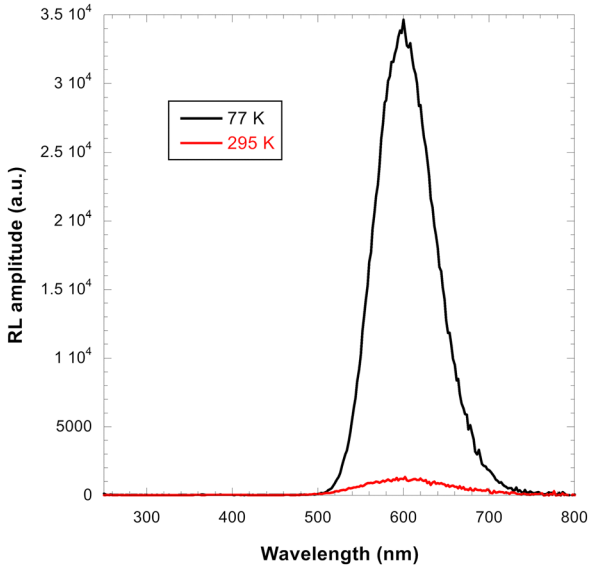

Fig. 9 RL spectra (Ex = 40 kV X-ray) of CTC measured at 77 K (black curve) and 295 K (red curve).

convolved with the instrumental response function, where $I(t)$, A_i and τ_i stand for intensity as a function of time t (expressed as the number of photons detected in the time interval), amplitude of the ith component and decay time of ith component, respectively. The so-called mean decay time was assessed, defined in a simple way:

$$\tau_{\text{mean}} = \sum_{i=1}^{n} \tau_i \text{LS}_i \quad (5)$$

where the light sum, LS, of the ith component is derived correspondingly:

$$\text{LS}_i = \frac{A_i \tau_i}{\sum_{i=1}^{n} A_i \tau_i} \quad (6)$$

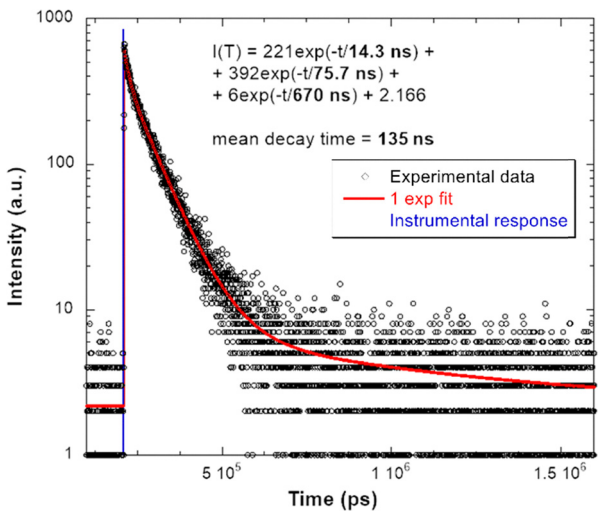

Fig. 10 Spectrally unresolved scintillation decay of CTC under the X-ray (40 kV) excitation measured at RT; LS1 = 9%, LS2 = 81%, LS3 = 10%.

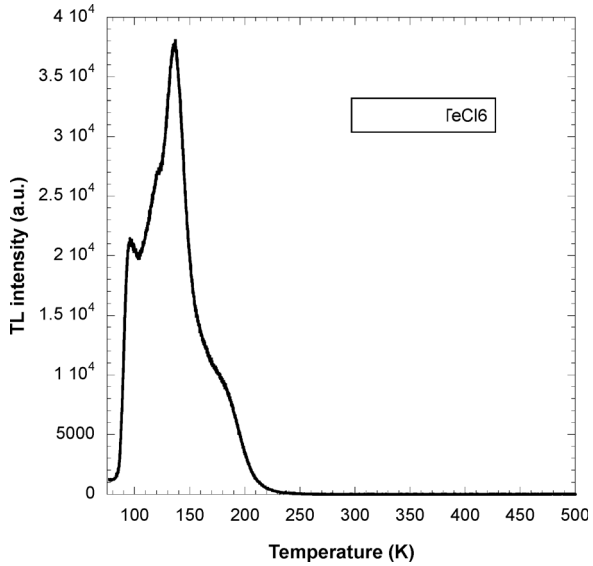

Fig. 11 TSL glow curves measured in the CTC powder sample.

The fastest component of the scintillation decay shows a decay time of 14.3 ns and a corresponding light sum of 9%, while the one with the highest light sum of 81% is characterized with the decay time of 75.7 ns close to that measured in PL decay in Fig. 6. These are followed by the low-amplitude slowest component on the order of hundreds of ns. The calculated mean decay time is then 135.3 ns.

4.5. Thermally stimulated luminescence (TSL) characteristics

Fig. 11 shows the TSL glow curve of CTC sample, irradiated by the 40 kV X-rays at 77 K. The shape of the TSL glow curve points to the presence of several strongly overlapped peaks of different intensities. The strongest ones were observed at 95 and 136 K with shoulders at about 119 and 185 K. Detrapping of the self-trapped and trapped holes from various sites is probably the key element in the TSL process, see EPR characteristics in Section 4.6.

4.6. EPR measurements

The defects contributing to TSL were further investigated by using EPR. Fig. 12 shows the EPR spectrum of CTC powder measured at 15 K, both before (blue solid line) and after irradiation at 405 nm and at a temperature of 15 K (green solid line). Prior to irradiation, the CTC powder exhibits a narrow spectral line at a magnetic field of 333.4 mT (with a g factor of 2.012), along with broad features of low intensity at lower and higher magnetic fields. These broad features are primarily attributed to the quartz tubes of the liquid helium cryostat. The narrow line, however, is clearly associated with the CTC powder itself. The positive shift in the g factor of this narrow line indicates that it originates from a hole-type center.

After irradiation, a new spectral feature appears primarily at the field range of 340–380 mT. This feature consists of several narrow spectral lines, resembling a hyperfine structure due to nuclear spin interactions, superimposed on a broad line. The observed hyperfine structure is similar to that of the paramagnetic Cl_2^- molecule (V_k center) described, for example, in ref. 44

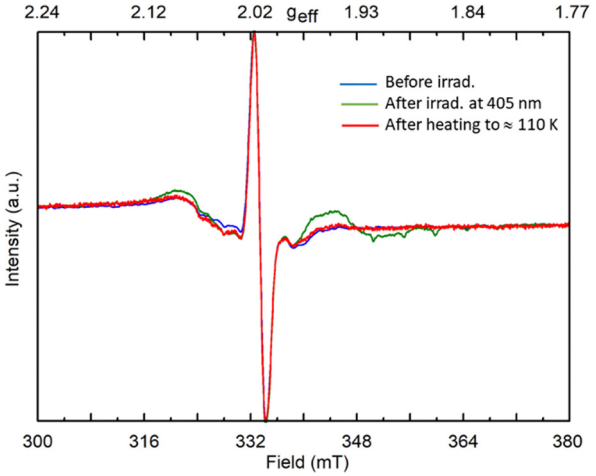

Fig. 12 EPR spectra of the CTC powder measured at 15 K. The blue solid line represents the spectrum before irradiation, the green line corresponds to the spectrum after irradiation at 405 nm and temperature 15 K, and the red solid line shows the spectrum after the irradiated powder was heated to approximately 110 K for 4 min and then cooled back to 15 K.

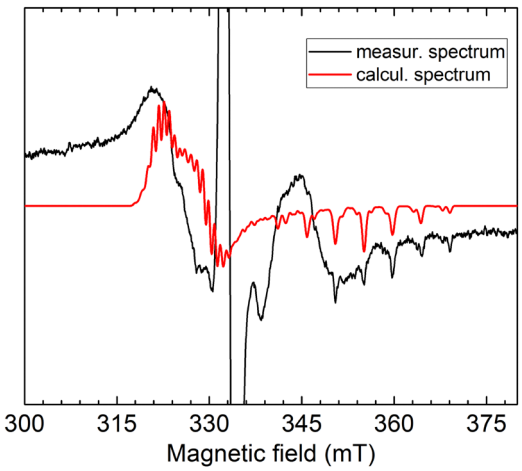

Fig. 13 Comparison of the measured (black solid line) and calculated spectra of the Cl_2^- molecule in Cs_2TeCl_6 powder irradiated at 405 nm.

for the similar compound Cs_2HfCl_6. To verify this assumption, we performed a simulation of the spectrum. The simulation was carried out using the following spin Hamiltonian:

$$H = g\beta BS + \sum_{i=1}^{2} SA_1^i I_1^i + \sum_{i=1}^{2} SA_2^i I_2^i, \quad (7)$$

where g is the g tensor, S is an electron spin operator with $S = 1/2$, I_1 (I_2) and A_1 (A_2) are the nuclear spins and hyperfine (HF) constants of the two $^{35,37}Cl$ isotopes. We employed the bispiral approach to determine the directions of crystallites homogeneously distributed within a sphere. For the search of resonance magnetic fields and transition probabilities for reference directions, HF interaction was treated as a perturbation to the magnetic Zeeman energy. The measured and calculated spectra are compared in Fig. 13. The simulated parameters are presented in Table 1. It is evident that the ^{35,37} Cl HF structure of the Cl_2^- molecule well describes the HF structure observed in the measured spectrum. As with other materials, the V_k center remains thermally stable up to about 70–80 K. Its spectrum completely disappears upon heating to the temperature 100–110 K for 4–5 min, as shown in Fig. 12.

Finally, it should be noted that the line at $g = 2.012$ may be attributed to an oxygen-related center, such as the O_2^- molecule or the O^- ion. However, determining its precise origin would require a separate study.

5. Conclusions

Cs_2TeCl_6 microcrystalline powders were prepared by using the hydrothermal method, an easy and fast way of preparing a large amount of the material. Electronic band structure calculations were performed by using GGA and LDA methods where the former provides the bandgap value of 2.76 eV, which is close to that of earlier literature data. From the electronic band structure, the effective mass of charge carriers was calculated and used further for the exciton diameter a_0 = 3.1 Å and finally exciton binding energy E_b = 1.5 eV calculations. The self-trapped exciton is ascribed to the observed luminescence band in agreement with previous literature. PL spectra and decay temperature dependences show a strong quenching of luminescence above 200 K which was assigned to simple thermal quenching to the ground state in contrast to a previous explanation based on the concentration quenching. The phenomenological two-excited-state level model provided an excellent fit for both the spectra integral and decay time temperature dependences over the broad temperature interval. The calculated energy barrier for the quenching process is 350 meV. Scintillation decay at room temperature is dominated by the component with the 75.7 ns decay time, close to that observed in PL decay. Such a fast scintillation response is promising for practical scintillation counting. Complex TSL glow curve points to several trapping sites acting in the process of energy transfer in the CTC lattice. EPR measurements identify the hole V_k center, *i.e.* self-trapped hole, as the key feature in the charge trapping. Exciton formation is then likely based on the V_k center attracting an electron from the conduction band followed by formation of an excitonic state. Future work is concerned with the embedding of CTC micro or nanocrystals

Table 1 Spin Hamiltonian parameters for the V_k centers in Cs_2TeCl_6 irradiated by 405 nm at 15 K and Cs_2HfCl_6 irradiated by X-rays at 77 K. The HF constants are given in units of 10^{-4} cm^{-1}

Material	g_x	g_y	g_z	$A_x(^{35}Cl)$	$A_y(^{35}Cl)$	$A_z(^{35}Cl)$	Thermal stability	Ref.
Cs_2TeCl_6	2.08(1)	2.02(1)	1.889(1)	8(2)	10(2)	41(1)	~70 K	This work
Cs_2HfCl_6	2.046(5)	2.046(5)	2.003(1)	10(2)	10(2)	85(2)	≈55 K	44

into a suitable host to create a bulk scintillation element which can be used in practical applications.

Author contributions

Lenka Prouzová Procházková – investigation, methodology, writing – original draft; Robert Král – writing – review & editing; Mikhail G. Brik – investigation – theoretical modelling, writing – original draft; Eva Mihóková – investigation – theoretical modelling, writing – review & editing; Romana Kučerková – investigation; Vítězslav Jarý – writing – review & editing, Vladimir Babin – investigation; František Hájek – investigation; Martin Nikl – supervision, funding acquisition, methodology, writing – review & editing.

Conflicts of interest

The authors declare no conflict of interest. The funders had no role in the design of the study; in the collection, analyses, or interpretation of data; in the writing of the manuscript, or in the decision to publish the results.

Data availability

The data related to figures are available upon request from the corresponding author.

Supplementary information (SI) is available. See DOI: https://doi.org/10.1039/d5tc04464b.

Acknowledgements

The support from the Horizon Europe EIC Pathfinder program through project 101098649 – UNICORN is gratefully acknowledged. Partial support was also obtained from OP JAC financed by ESIF and the MEYS, project SENDISO-CZ.02.01.01/00/22_008/0004596 and the Czech Science Foundation, Grant Number GA23-05615S. V. Laguta is acknowledged for EPR measurements performance and related data interpretation.

References

1 Y. Gao, Y. Pan, F. Zhou and G. Niu, *J. Mater. Chem. A*, 2021, **9**, 11931, DOI: 10.1039/d1ta01737c.
2 S. Ghosh, H. Shankar and P. Kar, *Mater. Adv.*, 2022, **3**, 3742, DOI: 10.1039/d2ma00071g.
3 L. Chu, W. Ahmad, W. Liu, J. Yang, R. Zhang, Y. Sun, J. Yang and X. Li, *Nano-Micro Lett.*, 2019, **11**, 16, DOI: 10.1007/s40820-019-0244-6.
4 D. Fabini, *J. Phys. Chem. Lett.*, 2015, **6**(18), 3546–3548, DOI: 10.1021/acs.jpclett.5b01747.
5 A. Babayigit, A. Ethirajan, M. Muller and B. Conings, *Nat. Mater.*, 2016, **15**, 247–251, DOI: 10.1038/nmat4572.
6 C. E. Torrence, C. S. Libby, W. Nie and J. S. Stein, *J. Phys. Chem. Lett.*, 2015, **6**, 3546–3548, DOI: 10.1016/j.isci.2022.105807.
7 T. Leijtens, G. E. Eperon, N. K. Noel, S. N. Habisreutinger, A. Petrozza and H. J. Snaith, *Adv. Energy Mater.*, 2015, **5**, 1500963, DOI: 10.1002/aenm.201500963.
8 A. Jana, S. Cho, A. Meena, A. T. A. Ahmed, V. G. Sree, Y. Park, H. Kim, H. Im and R. A. Taylor, *InfoMat*, 2024, **6**(12), e12559, DOI: 10.1002/inf2.12559.
9 K. Děcká, F. Pagano, I. Frank, I. N. Kratochwil and N. E. Mihóková, *J. Mater. Chem. C*, 2022, **35**(1), 1–7, DOI: 10.1039/d2tc02060b.
10 C. X. Ran, W. Y. Gao, J. R. Li, J. Xi, L. Li, J. F. Dai, Y. G. Yang, X. Y. Gao, H. Dong, B. Jiao, I. Spanopoulos, C. D. Malliakas, X. Hou, M. G. Kanatzidis and Z. X. Wu, *Joule*, 2019, **3**, 3072–3087, DOI: 10.1016/j.joule.2019.08.023.
11 A. E. Maughan, A. M. Ganose, M. M. Bordelon, E. M. Miller, D. O. Scanlon and J. R. Neilson, *J. Am. Chem. Soc.*, 2016, **138**(27), 8453–8464, DOI: 10.1021/jacs.6b03207.
12 M. G. Brik and I. V. Kityk, *J. Phys. Chem. Solids*, 2011, **72**, 1256–1260, DOI: 10.1016/j.jpcs.2011.07.016.
13 B. Lee, C. C. Stoumpos, N. J. Zhou, F. Hao, C. Malliakas, C. Y. Yeh, T. J. Marks, M. G. Kanatzidis and R. P. H. Chang, *J. Am. Chem. Soc.*, 2014, **136**, 15379–15385, DOI: 10.1021/ja508464w.
14 A. E. Maughan, A. M. Ganose, D. O. Scanlon and J. R. Neilson, *Chem. Mater.*, 2019, **31**, 1184–1195, DOI: 10.1021/acs.chemmater.8b05036.
15 L. Zhou, J. F. Liao, Z. G. Huang, X. D. Wang, Y. F. Xu, H. Y. Chen, D. B. Kuang and C. Y. Su, *ACS Energy Lett.*, 2018, **3**, 2613–2619, DOI: 10.1021/acsenergylett.8b01770.
16 R. Zeng, K. Bai, Q. Wei, T. Chang, J. Yan, B. Ke, J. Huang, L. Wang, W. Zhou, S. Cao, J. Zhao and B. Zou, *Nano Res.*, 2021, **14**, 1551–1558, DOI: 10.1007/s12274-020-3214-x.
17 E. Mihokova, V. Nagirnyi, M. Nikl, A. Stolovich, G. P. Pazzi, S. Zazubovich and V. J. Zepelin, *J. Phys.: Condens. Matter*, 1996, **8**, 4301–4314, DOI: 10.1088/0953-8984/8/23/020.
18 G. Blasse, G. J. Dirksen and W. Abriel, *Chem. Phys. Lett.*, 1987, **136**, 460–464, DOI: 10.1016/0009-2614(87)80287-7.
19 L. Zi, W. Xu, Z. Song, R. Sun, S. Liu, T. Xie, J. Zhu, S. Lu and H. Song, *J. Mater. Chem. C*, 2023, **11**, 2695, DOI: 10.1039/d2tc05153b.
20 R. Sa, Y. Wei, W. Zha and D. Liu, *Chem. Phys. Lett.*, 2020, **754**, 137538, DOI: 10.1016/j.cplett.2020.137538.
21 Y. Yao, S. W. Zhang, L. Ma, G. Wei, Z. Liu, C. Y. Wang and F. Kanga, *RSC Adv.*, 2021, **11**, 26415, DOI: 10.1039/d1ra10.1016/j.sna.2023.11415303622j.
22 M. X. Chong, C. T. Li, L. X. Zhang and L. J. Bie, *Sens. Actuators, A*, 2023, **351**, 114153, DOI: 10.1016/j.sna.2023.114153.
23 Z. Tan, Y. Chu, J. Chen, J. Li, G. Ji, G. Niu, L. Gao, Z. Xiao and J. Tang, *Adv. Mater.*, 2020, **32**, 2002443, DOI: 10.1002/adma.202002443.
24 P. Cheng, D. Zheng, L. Feng, Y. Liu, J. Liu, J. Li, Y. Yang, G. Wang and K. Han, *J. Energy Chem.*, 2022, **65**, 600, DOI: 10.1016/j.jechem.2021.06.033.
25 J. Lai, P. Wang, B. Zheng, T. Xuan, D. Wu, Z. Wang, Y. Wang, W. Zhang, J. Du, P. He, K. An and X. Tang, *Adv. Opt. Mater.*, 2024, **12**, 2303297, DOI: 10.1002/adom.202303297.

26 A. P. Meshik, C. M. Hohenberg, O. V. Pravdivtseva, T. J. Bernatowicz and Y. S. Kapusta, *Nucl. Phys. A*, 2008, **809**, 275–289, DOI: 10.1016/j.nuclphysa.2008.06.010.
27 W. J. Lin, O. K. Manuel, S. Muangnoicharoen and R. I. Thorpe, *Nucl. Phys. A*, 1988, **481**, 484–493, DOI: 10.1016/0375-9474(88)90341-7.
28 D. J. Auty, D. Bartlett, S. D. Biller, D. Chauhan, M. Chen, O. Chkvorets, S. Connolly, X. Dai, E. Fletcher, K. Frankiewicz, D. Gooding, C. Grant, S. Hall, D. Horne, S. Hans, B. Hreljac, T. Kaptanoglu, B. Krar, C. Kraus, T. Kroupova, I. Lam, Y. Liu, S. Maguire, C. Miller, S. Manecki, R. Rosero, L. Segui, M. K. Sharma, S. Tacchino, B. Tam, L. Tian, J. G. C. Veinot, S. C. Walton, J. J. Weigand, A. Wright, M. Yeh and T. Zhao, *Nucl. Instrum. Methods Phys. Res., Sect. A*, 2023, **1051**, 168204, DOI: 10.1016/j.nima.2023.168204.
29 P. Engel, *Z. Kristallogr. – Cryst. Mater.*, 1935, **90**, 341–373, DOI: 10.1524/zkri.1935.90.1.341.
30 M. D. Segall, P. J. D. Lindan, M. J. Probert, C. J. Pickard, P. J. Hasnip, S. J. Clark and M. C. Payne, *J. Phys.: Condens. Matter*, 2002, **14**, 2717–2744, DOI: 10.1088/0953-8984/14/11/301.
31 *Material Studio Release Notes, Release 6.1*, Accelrys Software Inc., 2012.
32 D. M. Ceperley and B. J. Alder, *Phys. Rev. Lett.*, 1980, **45**, 566–569, DOI: 10.1103/PhysRevLett.45.566.
33 J. P. Perdew, K. Burke and M. Ernzerhof, *Phys. Rev. Lett.*, 1996, **77**, 3865–3868, DOI: 10.1103/PhysRevLett.77.3865.
34 M. A. Ali, T. Alshahrani and G. Murtaza, *Mater. Sci. Semicond. Process.*, 2021, **127**, 105728, DOI: 10.1016/j.mssp.2021.105728.
35 K. Bouferrache, M. A. Ghebouli, B. Ghebouli, M. A. Habila, T. Chihi, M. Fatmi, A. Djemli and M. Sillanpaa, *Results Phys.*, 2024, **56**, 107138, DOI: 10.1016/j.rinp.2023.107138.
36 P. Y. Yu and M. Cardona, Electronic properties of defects, *Fundamentals of Semiconductors: Physics and Materials Properties*, Berlin, Heidelberg, Springer, Berlin Heidelberg, 1996.
37 L. Protesescu, S. Yakunin, M. I. Bodnarchuk, F. A. Krieg, R. Caputo, C. H. Hendon, R. X. Yang, A. Walsh and M. V. Kovalenko, *Nano Lett.*, 2015, **15**, 3692–3696, DOI: 10.1021/nl5048779.
38 B. Zhu, X. Chen and X. Cui, *Sci. Rep.*, 2015, **5**, 9218, DOI: 10.1038/srep09218.
39 S. Smolenski, M. Wen, Q. Li, E. Downey, A. Alfrey, W. Liu, A. L. N. Kondusamy, A. Bostwick, C. Jozwiak, E. Rotenberg, L. Zhao, H. Deng, B. Lv, D. Zgid, E. Gull and N. H. Jo, *Nat. Commun.*, 2025, **16**, 1134, DOI: 10.1038/s41467-025-56457-x.
40 J.-H. Choi, P. Cui, H. Lan and Z. Zhang, *Phys. Rev. Lett.*, 2015, **115**, 066403, DOI: 10.1103/PhysRevLett.115.066403.
41 M. N. Amar, M. A. Ghriga, M. E. A. B. Seghier and H. Ouaer, *J. Phys. Chem. B*, 2020, **124**, 6037–6045, DOI: 10.1021/acs.jpcb.0c04259.
42 J. Becker, J. Y. Gesland, N. Yu Kirikova, J. C. Krupa, V. N. Makhov, M. Runnea, M. Queffelec, T. V. Uvarova and G. Zimmera, *J. Alloys Compd.*, 1998, **205**, 275–277, DOI: 10.1016/S0925-8388(98)00304-1.
43 M. Yokota and O. Tanimoto, *J. Phys. Soc. Jpn.*, 1967, **22**, 779–784, DOI: 10.1143/JPSJ.22.779.
44 R. Kral, B. Babin, E. Mihokova, M. Buryi, V. V. Laguta, K. Nitsch and M. Nikl, *J. Phys. Chem. C*, 2017, **121**, 12375, DOI: 10.1021/acs.jpcc.7b02327 EPR spectra were simulated using the "Visual EPR" programs by V. Grachev (https://www.visual-epr.com).